INFLUENCE OF STEEL ALLOY COMPOSITION ON THE PROCESS ROBUSTNESS OF AS-BUILT HARDNESS IN LASER-DIRECTED ENERGY DEPOSITION

J. P. Kelley[1], J. W. Newkirk[2], L. N. Bartlett[3], T. Sparks[4], S. P. Isanaka[1], S. Alipour[3], and F. Liou[1,4]

[1]Department of Mechanical and Aerospace Engineering
[2]Department of Nuclear Engineering and Radiation Science
[3]Department of Materials Science and Engineering
Missouri University of Science and Technology, Rolla, MO 65401
[4]Product Innovation and Engineering LLC, St. James, MO 65559

Abstract

To ensure consistent quality of additively manufactured parts, it is advantageous to identify alloys which can meet performance criteria while being robust to process variations. Toward such an end, this work studied the effect of steel alloy composition on the process robustness of as-built hardness in laser-directed energy deposition (L-DED). In-situ blending of ultra-high-strength low-alloy steel (UHSLA) and pure iron powders produced 10 alloys containing 10-100% UHSLA by mass. Thin-wall samples were deposited, and the hardness sensitivity of each alloy was evaluated with respect to laser power and interlayer delay time. The sensitivity peaked at 40-50% UHSLA, corresponding to phase fluctuations between lath martensite and upper bainite depending on the cooling rate. Lower (10-20%) or higher (70-100%) alloy contents transformed primarily to ferrite or martensite, respectively, with auto-tempering of martensite at lower cooling rates. By avoiding martensite/bainite fluctuations, the robustness was improved.

Keywords: Laser-directed energy deposition, alloy design, robustness, sensitivity analysis, high-strength low-alloy steel, in-situ alloying, powder blend

Introduction

Additive manufacturing (AM), commonly known as 3D printing, has received growing attention for its ability to rapidly fabricate complex-shaped parts. In AM, components are built in a layer-by-layer fashion directly from a computer-generated 3D model. Among the AM processes available for metals, two of the most common are laser-powder bed fusion (L-PBF), also known as selective laser melting (SLM), and laser-directed energy deposition (L-DED). In L-PBF, each layer of the part is defined by selectively melting a region within a thin layer of metal powder spread onto a base plate [1]. In L-DED, a laser generates a melt pool on the surface of a substrate, and a metal feedstock in wire or powder form is injected through a nozzle into the melt pool. Individual tracks are deposited adjacent to one another to form a layer, and successive layers are added until the part is complete [2]. Metal AM is particularly advantageous for low-quantity production of complex parts, with applications often found in aerospace, biomedical, and energy sectors [3].

Although metal AM offers many advantages, it comes with its own set of challenges. AM has much in common with multi-pass welding; both processes lead to rapid cooling rates and complex thermal histories [4, 5]. Some alloys are naturally conducive to AM, while others are

very challenging to deposit without defects. The term "printability" (similar to weldability) refers to how readily a material can be printed without defects such as porosity or solidification cracking [5–7]. In addition to printability concerns, input parameters including laser power, scan speed, hatch spacing, and powder feed rate, as well as part size and geometry, all work together to influence the thermal history, which in turn impact the properties of the final build [2, 4, 5, 8, 9]. To ensure consistent quality, there is a need to identify alloys which are robust to process variations. This is particularly critical if the alloy is to be used in multiple types of AM processes, as cooling rates can vary widely from L-PBF ($\sim10^4$-10^6 °C/s [10]) to L-DED ($\sim10^3$-10^4 °C/s [8]) to wire-arc AM (~100 °C/s [11]). A robust system is one whose output is relatively insensitive to changes in "noise" variables. Robustness is achieved by tuning the set of available control factors such that the noise factors have minimal impact on the output [12–14]. The optimal system achieves the desired output while being robust to noise, as depicted by the purple line in Figure 1.

Many studies have used AM with existing alloys such as 316L stainless steel, Ti-6Al-4V, and Inconel 718 [9]. Relatively fewer efforts have been aimed at designing alloys for AM processes. Within alloy design for AM, a range of studies have focused on printability [5–7, 15–18] or grain refinement [19, 20]. In-situ alloying of blended powders [7, 21–23], Integrated Computational Materials Engineering (ICME), finite element modeling, and machine learning have been used as tools for alloy design [6, 7, 17, 22]. A few studies have made strides toward applying robustness concepts to AM alloy design. Haines *et al.* (2018) studied the effect of alloy composition on the columnar-to-equiaxed transition (CET) of Ni-based superalloys, with the goal of promoting equiaxed grain structures across a wide range of processing conditions [20]. Johnson *et al.* (2019) used a model to develop printability maps for two alloys, with the size of the printable processing window serving as a metric for robustness [16]. Wang *et al.* (2020) used an ICME framework to design an optimized variation of the high-strength low-alloy steel HSLA-115 under compositional uncertainty [15]. Other authors have applied robust design perspectives to the improvement of AM processes [12, 24, 25] or conducted sensitivity studies on specific alloys [26–28].

Assessing the above literature, there seems to be a lack of dedicated studies investigating the process robustness of mechanical properties and microstructural phases over a wide composition space. Hence, the present work investigates the effect of steel alloy composition on the robustness of as-built hardness to process variations in powder-based L-DED. The alloying elements were the control factors, while the processing parameters were treated as "noise" factors. A two-feeder system was used to blend ultra-high-strength low-alloy steel (UHSLA) and pure iron powders in-situ, producing 10 compositions containing 10-100% UHSLA in increments of 10% by mass. Thin-wall samples were deposited, and the hardness sensitivity of each alloy was evaluated with respect to laser power and interlayer delay time. The artificial interlayer delay mimics the time taken for the laser to return to a particular point within a larger build. Microstructural phases were characterized and correlated with the hardness results. Primary goals of this research were 1) to gain an understanding of key mechanisms underlying robustness differences among steel alloys in L-DED and 2) to develop and assess a novel approach for incorporating robust design into the rapid evaluation of alloys for metal AM.

Quantifying Robustness

Robustness is closely related to variability, as a more robust system will result in less variability of the output in the presence of noise factors (Figure 1a). Hence, the standard deviation is one simple metric for evaluating robustness. While the standard deviation quantifies variability, it does not provide insight into the cause of such variability. To assess an output's response to a given set of input factors, a design of experiments (DOE) methodology coupled with multiple linear regression can be employed, resulting in an input-output relationship as follows [29]:

$$y = \beta_0 + \beta_1 x_1 + \beta_2 x_2 + \ldots + \beta_n x_n \tag{1}$$

In Equation 1, y represents the output variable, β_0 represents y-intercept, x_1-x_n represent each of the n input variables, and β_1-β_n represent the coefficients corresponding to the input variables. A given coefficient β_i represents the "slope" of the input-output relationship with respect to a given input variable x_i with all other input variables held constant [29]. As the input variables x_i potentially have different units, the β_i coefficients must be scaled before the relative influences of the input factors can be compared directly. JMP Pro statistical analysis software (used in this study) calculates a "scaled coefficient" for each input, which quantifies how much the output changes as an input traverses half its range [30]. This is illustrated in Figure 1b for a single-input system. While the scaled coefficient relates to the *slope* of an input-output relationship, the LogWorth indicates whether the relationship can be considered *statistically significant* given the data. The LogWorth is equal to $-\log_{10}$(p-value). Higher LogWorth (i.e., lower p-value) indicates higher statistical significance of the input-output relationship. A LogWorth>1.3, which corresponds to a p-value<0.05, is required for a given input's effect to be considered statistically significant to a significance level $\alpha = 0.05$ [31, pp. 66-81].
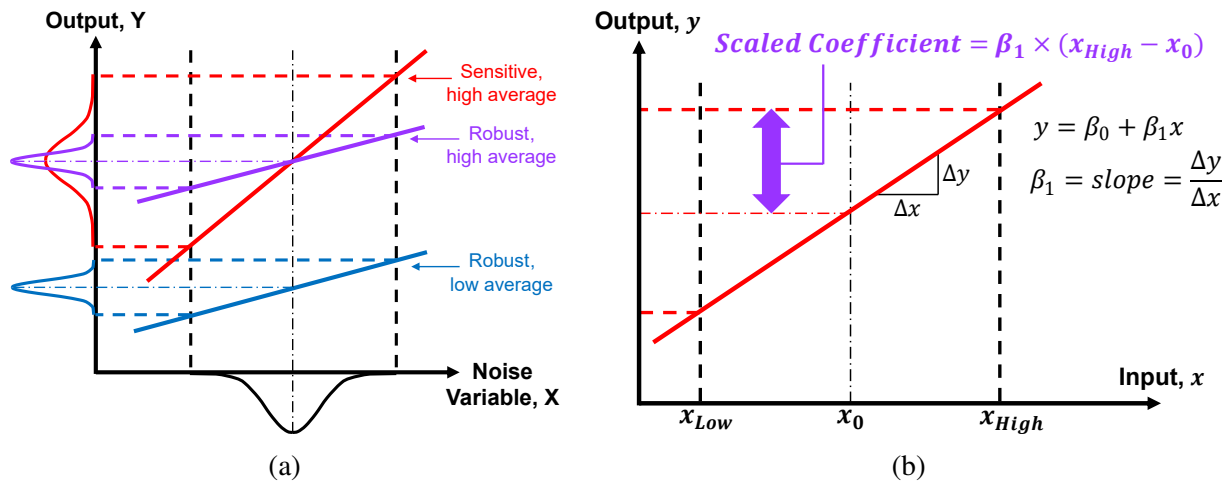

Figure 1. (a) Robust vs. sensitive outputs, (b) calculation of scaled coefficient.

In this study, then, an improvement in robustness (i.e., reduction in sensitivity) is considered to correspond to a decrease in the standard deviation and scaled coefficients, where the scaled coefficients represent the impacts of laser power and interlayer delay on the Vickers hardness for a particular alloy. The LogWorth is used to evaluate the statistical significance of the inputs.

Experimental Procedures

Materials and Equipment

The UHSLA and pure iron powders (gas-atomized) were purchased from Powder Alloy Corporation (PAC) and Atlantic Equipment Engineers (AEE), respectively. The chemical compositions as reported by the suppliers are provided in Table 1. The as-received UHSLA powder was sieved to obtain a particle size range of ~75-106 μm. The iron powder was sieved to remove particles below 53 μm. Three static light scattering (SLS) measurements were averaged to obtain the particle size distributions (PSDs) of the powders. Figure 2 provides scanning electron microscope (SEM) images, optical images, and PSDs of the two powders after sieving. Note the surface oxidation on the UHSLA powder and the porosity inside both powders. The average D10/D50/D90 after sieving were 59.0/76.8/103.2 μm for UHSLA and 49.3/69.6/100.9 μm for the pure iron powder.

Table 1. Chemical composition (wt%) of UHSLA and pure iron powders.

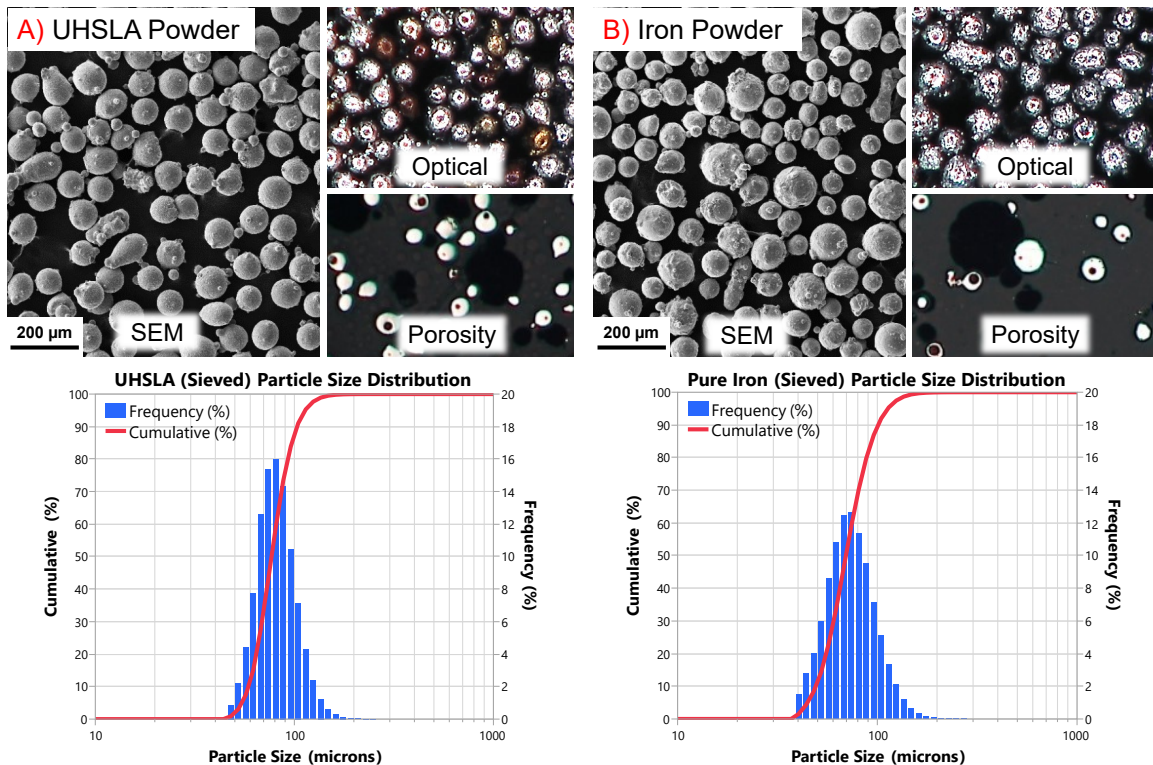| Element	Fe	Cr	Ni	Mo	Si	Mn	C	V	Cu
UHSLA	Balance	2.8	1.1	1	0.9	0.7	0.28	0.12	<0.1
Pure Iron	99.89% min	0.0295	0.008	0.001	0.0001	0.012	0.0075		0.0095
Element	O	P	Al	S	Ti	H	N	W	
UHSLA	0.028	<0.010	<0.009	<0.005	0.004	0.0002			
Pure Iron	431 ppm				0.0038		63 ppm	0.042	

Figure 2. Images and PSD - (a) sieved UHSLA powder, (b) sieved iron powder.

The L-DED system is depicted in Figure 3. The system used a TeraDiode DLS-0970-02000-DBS direct-diode laser (wavelength 978 nm) with 2-kW maximum output power, tilted 15° from vertical. A Nachi MZ07 6-axis robot controlled the movement of the substrate. The UHSLA and pure iron powders were metered from an electrostatically-cleared wheel feeder and vibrational feeder, respectively, both manufactured by Powder Motion Labs. The two powder lines were converged downstream to mix the powders in-situ. The blended stream was then split between two nozzles until intersecting the laser beam at the melt pool (Figure 3a). A novel rotary setup was used in which thin-wall samples were deposited around the circumference of a cylindrical substrate clamped by the robot (Figure 3b/3c). This allowed multiple deposits to fit within a small space, minimizing the time required for mounting and polishing after deposition. A pyrometer inside the robot wrist monitored the temperature of the clamped end of the substrate.
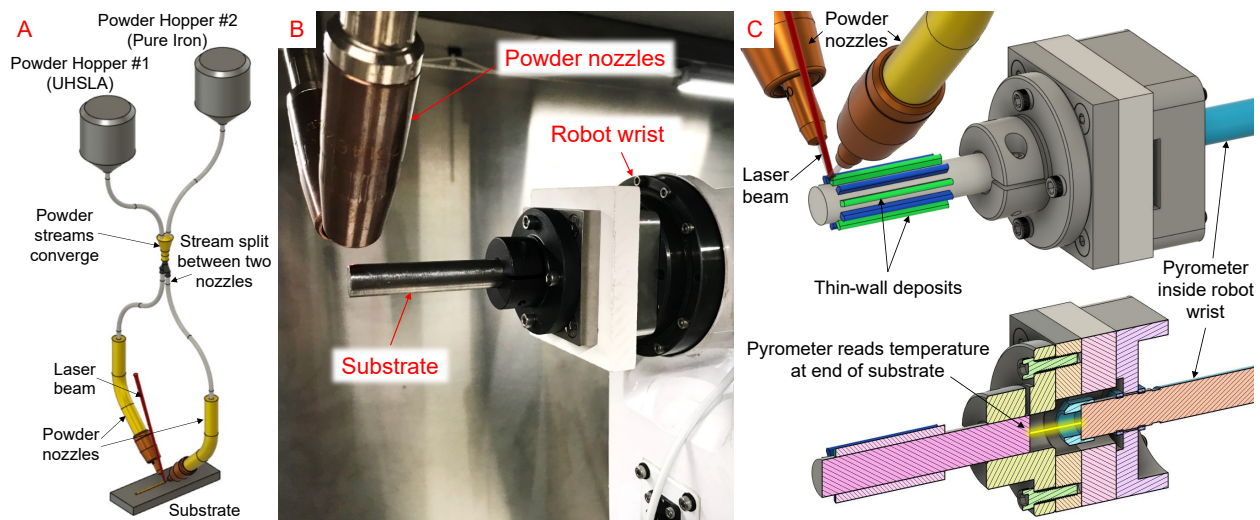
Figure 3. L-DED setup - (a) powder delivery, (b) rotary system photo, (c) rotary system 3D model.

Hardness Experiments

Following a Design of Experiments (DOE) methodology, a 2-factor, 2-level experiment (plus 1 center point) was employed to assess the impact of laser power and interlayer delay time on the as-built hardness of 10 different alloy compositions. $2^2+1=5$ total combinations of input factors. Two replicates of the experiment, each with a different randomized run order, were carried out using a single substrate for each composition. Within a replicate, 5 thin-wall samples were deposited corresponding to the 5 factor level combinations, with a 2-minute pause between deposits. Before beginning replicate 2, the substrate was allowed to cool to ~30 °C. Figure 4a illustrates the deposition strategy for each individual thin wall as viewed from the side. Figure 4b depicts the radial location of the 10 deposits as viewed from the end. The samples were deposited in a star-like fashion around the circumference of the substrate, with the numbers 1-5 corresponding to the runs in Table 2. The samples in replicate 2 were deposited between those of replicate 1. The star-like pattern was employed in an effort to balance out the heat input around the substrate.

For all deposits, the scan speed was 10 mm/s, and the total powder feed rate was 2.5 g/min. The individual feed rates of the UHSLA and iron powders determined the composition, which

ranged from 10-100% UHSLA in increments of 10% by mass. Argon carrier and shield gas were run at 0.12 L/min through each powder line and 3.0 L/min around each nozzle, respectively. The substrate material was 1018 low-carbon steel with dimensions 3" long × 0.5" in diameter. The deposit length was 40 mm, plus a 5-mm distance on either end in which the laser was turned off while the robot decelerated and accelerated to move to the next layer, ensuring constant velocity within the deposited area. Note the interlayer delay includes the time required to travel this 5-mm distance back and forth. 20 layers were deposited with a 0.15-mm Z-increment between each layer, giving a total deposit height of about 3.0 mm. The wall thickness was ~1.5-2.5 mm depending on the laser power, with higher laser powers giving wider tracks. A single preheat pass was run at a laser power of 1050 W. The first 2 layers were deposited with 1050-W laser power and 1-second interlayer delay to ensure adequate bonding with the substrate. The remaining 18 layers were deposited using the laser power and interlayer delay dictated by the experimental run in Table 2.
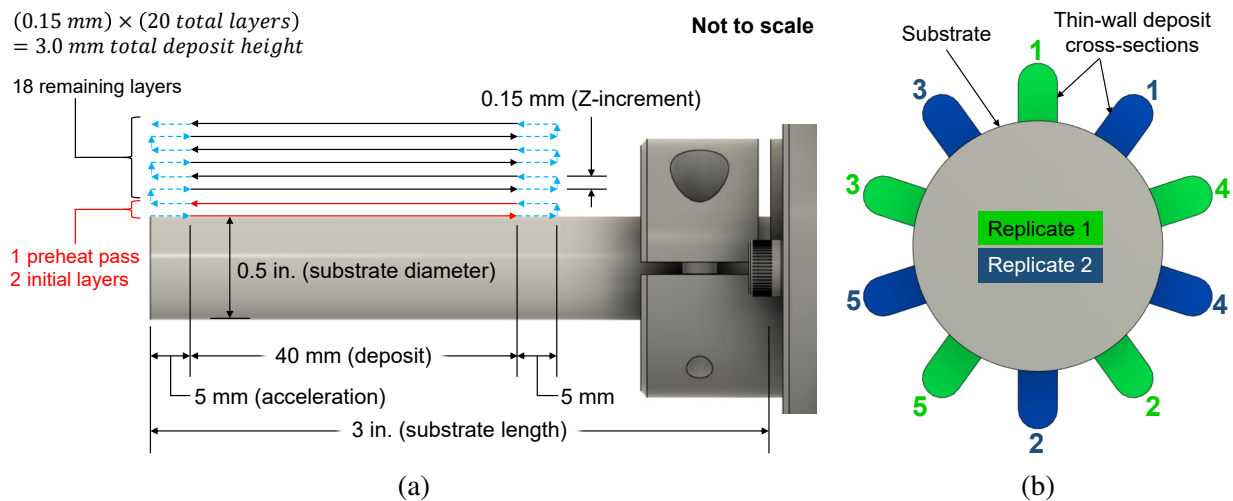

Figure 4. Thin-wall deposition strategy - (a) side view, (b) end view depicting deposit order.

Table 2. Thin-wall rotary deposition DOE (randomized).

Replicate	1					2				
Run	1	2	3	4	5	1	2	3	4	5
Laser Power (W)	650	1050	850	1050	650	650	1050	650	850	1050
Interlayer Delay (s)	11	1	6	11	1	1	11	11	6	1

The completed experiments resulted in 10 substrates corresponding to the 10 compositions, each containing 10 deposits corresponding to the 10 experimental runs (5 runs each replicate). Figure 5a shows an example of a completed sample after being sectioned for hardness and microstructure analysis, with the analyzed surface located at about the middle of the deposit length. The cut-out sections were hot-mounted and polished to a 0.25-μm finish. A METPREP 3 PH-3 machine and consumables by Allied High Tech Products were used for grinding and polishing. The grinding sequence (grit size) was 120-240-320-400-600-800-1200 using SiC sandpaper. The polishing sequence (microns) was 6-3-1-0.5-0.25 using a glycol-based diamond suspension for the first 3 steps and a diamond paste with BlueLube polishing lubricant for the last 2 steps.
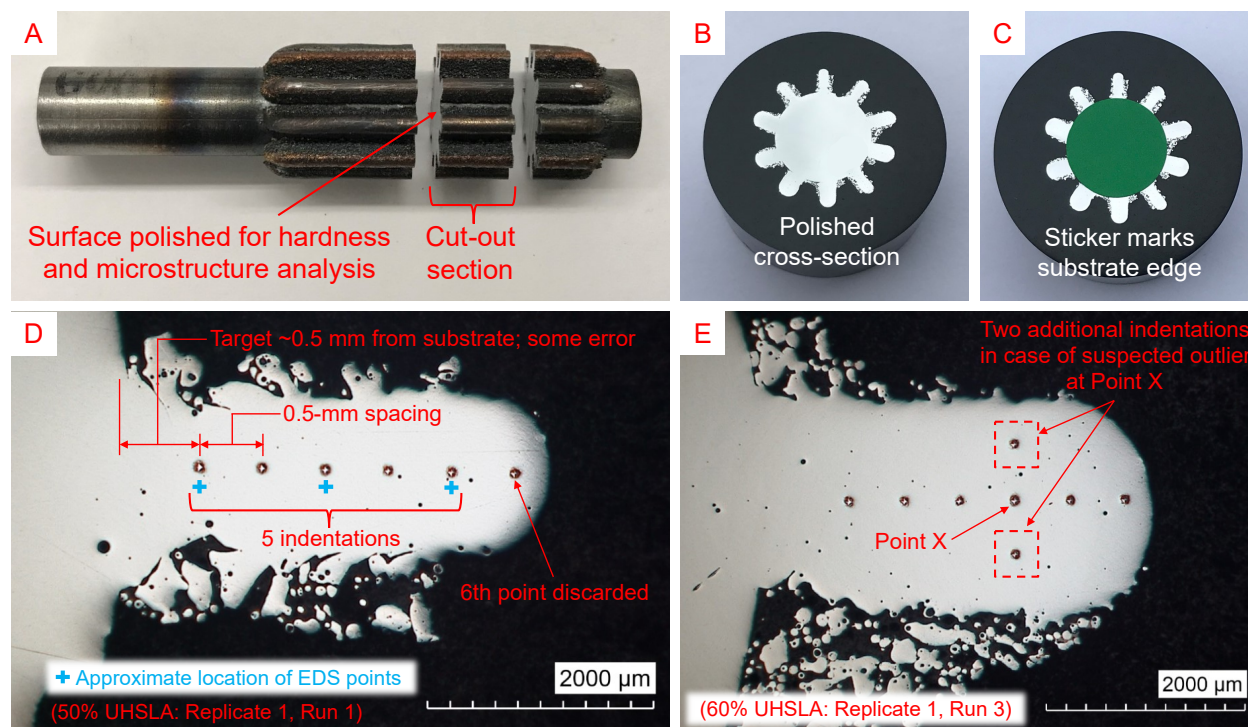
Figure 5. (a) Example of substrate containing 10 thin-wall deposits, (b) example of polished cross-section, (c) sticker added to mark substrate edge, (d) hardness indentation layout, (e) extra indentations in case of suspected outlier.

One of the polished cross-sections is shown in Figure 5b. A sticker was applied to the center of each sample to mark the edge of the substrate (Figure 5c). 5 Vickers hardness indentations were made along the build direction of each thin-wall cross-section, beginning near the substrate and moving outward as shown in Figure 5d. A 0.5-mm spacing was targeted between the substrate and the first indentation to avoid hitting the 2 initial layers which had been deposited using a higher laser power. Due to slight errors in the placement of the stickers, there was a degree of error in locating the first indentation. The remaining indentations were spaced 0.5 mm apart, maintaining the required spacing of at least 2.5 times the diagonal length of each indentation as per ASTM standard E92-17 [32]. Although some deposits were tall enough to permit a 6th indentation, this point was discarded to maintain a consistent number of data points analyzed for each deposit.

One of the deposits – 10% UHSLA, replicate 1, run 2 – contained an unusually large pore allowing space for only 3 indentations. Aside from this sample, all deposits contained 5 indentations which were used in the subsequent analyses. 5 indentations × 10 deposits per composition × 10 compositions = ~500 total indentations. Note that out of this total, 5 indentations were too close to the sample's outer edge to meet ASTM E92-17 [32]. Nevertheless, these measurements were included in the dataset, as they did not significantly deviate from the other measurements. In a few cases, the hardness measured at a particular point (designated Point X in Figure 5e) was unusually low compared to the 4 neighboring measurements or had a deformed shape, possibly indicating the indenter had hit a pore, compositional inhomogeneity, or other defect. In such cases, two additional measurements on either side of Point X were averaged and used instead of Point X.

Multiple linear regression (standard least squares) was performed on the hardness data from each composition using JMP Pro statistical analysis software to assess the hardness response to the input factors. After hardness measurement, each sample was etched by dipping in a 2% Nital solution for 10-15 seconds. Microstructures were viewed under an optical microscope (OM) and scanning electron microscope (SEM), specifically an Axia ChemiSEM by ThermoFisher Scientific.

To check whether the in-situ powder mixing strategy had achieved the target compositions, energy dispersive spectroscopy (EDS) via the Axia ChemiSEM was used to estimate the average alloying element content (wt%) in each sample. Note that EDS readings are typically not very accurate for very low alloy contents such as those in low-alloy steels. The purpose of these measurements was not to obtain an accurate absolute reading, but rather to check the *trend* in the element contents as more iron powder was added to the mixture. An EDS line scan consisting of 3 points was conducted for each deposit, with each point located near one of the hardness indentations as indicated by the blue "+" signs in Figure 5d. 3 points per deposit × 10 deposits per composition = 30 total EDS readings per composition. The 7 elements Fe, C, Si, Cr, Mn, Ni, and Mo were included in the analysis, corresponding to the primary elements in the UHSLA steel. The collection time was 60 seconds per point using an acceleration voltage of 15 kV and spot size 7.0-9.0, achieving an average count rate well above 100,000 counts/second for most points.

Results & Discussion

EDS Analysis

The EDS analysis results are plotted in Figure 6. The graphs show the measured weight percentages of Cr, Ni, Si, Mo, and Mn. The solid lines represent the average EDS readings, with error bars representing the standard deviation in the 30 measurements for each composition. The dotted lines represent the target composition. Since the purpose of the EDS measurements was to assess the *trends* in the element contents, the "target" element content for a particular alloy was set *relative* to the content *measured* via EDS for 100% UHSLA. For example, if the average Cr content for 100% UHSLA was measured to be 3.0 wt%, the target Cr content for 70% UHSLA was calculated as $(70/100) \times 3.0$ wt% = 2.1 wt%.

Overall, the observed trends suggest the in-situ mixing strategy was effective in achieving approximately the target compositions. As evident in Figure 6, the measured element contents generally fall relatively close to the target, following a linear trend with respect to the %UHSLA in the mixture. In particular, the measured Cr content tracks very well with the target, and the trends for Ni and Si show good linearity. The measured Mo and Mn contents exhibit more variability, possibly because the quantities of these elements are especially low, leading to more difficulty in obtaining an accurate reading. The EDS reading of the carbon content (not shown) was much too high at ~4.25-5.50 wt%, possibly due to organic contamination on the sample.

Temperature History

Figure 7 plots the temperature history recorded by the pyrometer at the clamped end of the substrate during deposition of all 10 thin walls for 100% UHSLA. The substrate temperature
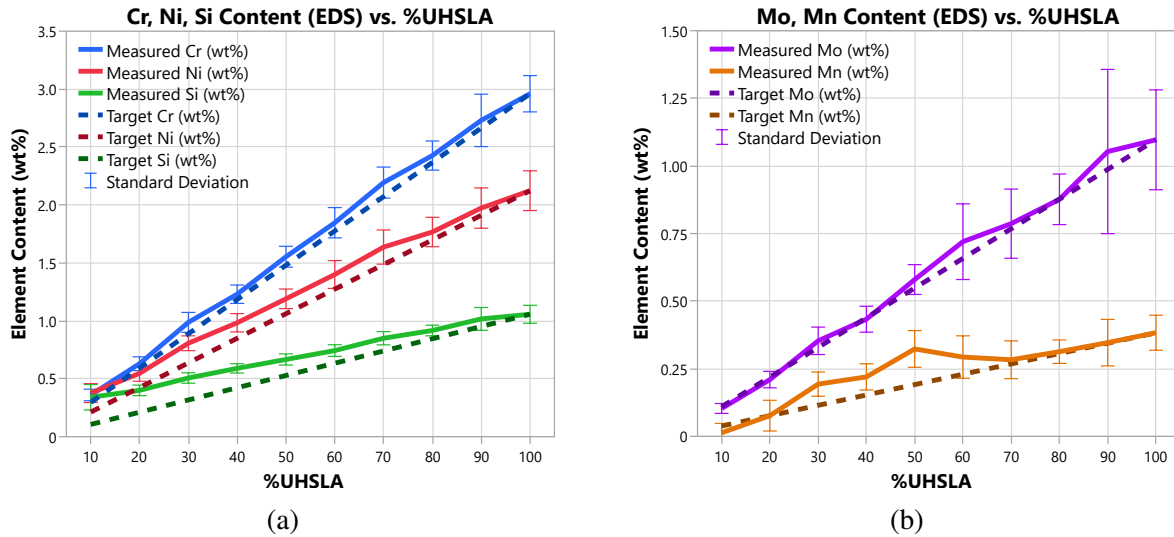
Figure 6. EDS measurements of alloying element content - (a) Cr, Ni, Si, (b) Mo, Mn.

histories for all compositions were similar. The 2 major peaks in temperature correspond to the two replicates, as the substrate was allowed to cool to ~30 °C before beginning replicate 2. Within each replicate, the substrate temperature naturally rose as each sample was deposited. The 5 minor peaks within each of the 2 major peaks correspond to the 5 deposits within each replicate. While the maximum temperature measured at the clamped end was only 150-160 °C, the substrate temperature very near to the deposit was likely much higher.
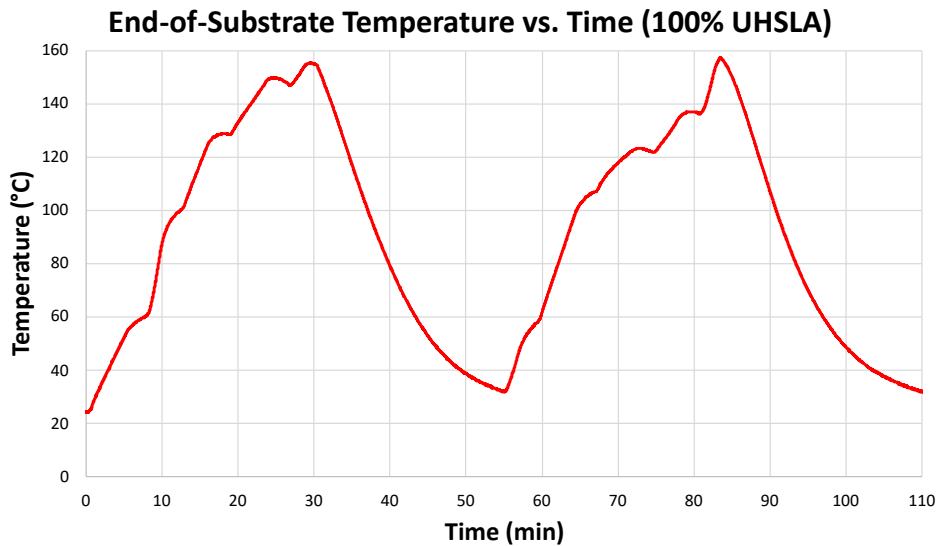

Figure 7. Temperature history at end of substrate (100% UHSLA).

A couple aspects of the temperature history are worth noting. First, deposits added later within a replicate had a higher starting substrate temperature. A higher preheat temperature leads to a lower thermal gradient between the substrate and the deposit, possibly decreasing the hardness

through reducing the cooling rate [33]. Second, previously-deposited thin walls could potentially have undergone tempering due to reheating as subsequent deposits were added nearby. Thus, in addition to the two input factors controlled in the experiment, it is possible that the run order had a degree of influence on the hardness due to depositing many samples on a single substrate.

Hardness Sensitivity

Figure 8 gives the mean Vickers hardness, standard deviation, and coefficient of variation (CV) for each composition, with both replicates included in the calculations. The CV is equal to the standard deviation divided by the mean (here expressed as a percentage), representing the variability in a dataset relative to its magnitude. Recall ~50 hardness measurements were taken for each composition. Table 3 summarizes the results. Conversions from average Vickers hardness (HV) to Rockwell C hardness (HRC) were done using equation A1.1.1 from ASTM standard E140-12B(2019) [34]. Note this conversion is only valid for ≥20 HRC.

As expected, the mean hardness increases with increasing %UHSLA (Figure 8a) due to the higher percentage of carbon and other alloying elements [35]. The standard deviation in the hardness data follows an interesting trend (bar chart in Figure 8b). Beginning at 10% UHSLA, the standard deviation increases until reaching a maximum at 40% UHSLA. Beyond this point, the standard deviation generally decreases as more UHSLA is added, with the notable exception of a substantial peak at 100% UHSLA and a smaller peak at 80% UHSLA. The CV exhibits a similar pattern as the standard deviation, peaking at 40% UHSLA and then dropping off as more UHSLA is added (purple line graph in Figure 8b). Because the CV is the standard deviation divided by the mean, the drop in the CV for UHSLA contents below 40% is less pronounced than the corresponding drop in the standard deviation, as the mean hardness decreases significantly as more iron is added. The behavior of the standard deviation seems to suggest an increased sensitivity to processing parameters at 40-50% UHSLA.
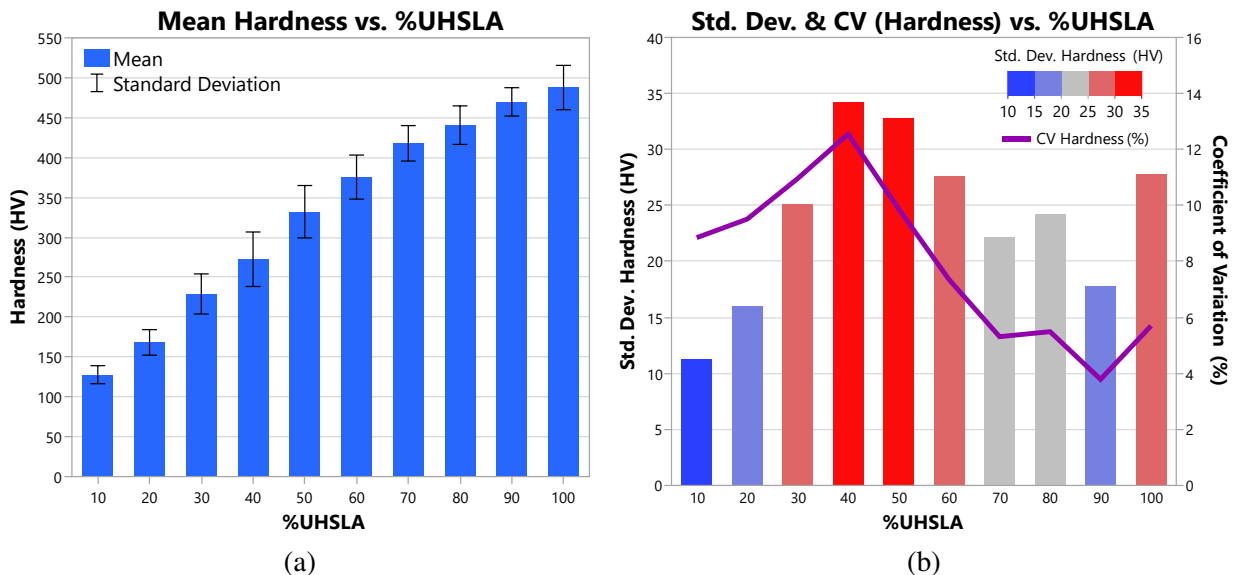

Figure 8. (a) Mean Vickers hardness, (b) standard deviation and coefficient of variation.

Table 3. Summary of hardness results (both replicates together).

%UHSLA	10	20	30	40	50	60	70	80	90	100
Mean Hardness (HV)	127.7	168.2	229.0	272.5	332.1	375.5	417.8	440.6	469.7	487.7
Std. Dev. Hardness (HV)	11.3	16.0	25.1	34.2	32.8	27.6	22.2	24.2	17.8	27.8
CV Hardness (%)	8.9	9.5	11.0	12.5	9.9	7.4	5.3	5.5	3.8	5.7
Mean Hardness (HRC)[*]	-	-	-	26	34	38	42	44	47	48

[*] Conversion to HRC only valid for ≥20 HRC [34].

To assess the impact of laser power and interlayer delay time on the as-deposited Vickers hardness of each composition, the LogWorth and scaled coefficients resulting from the multiple linear regression analyses are plotted in Figures 9 and 10, respectively. Higher LogWorth (lower p-value) only implies stronger evidence that a correlation *does exist*; it does *not* measure the size of the response [36]. The scaled coefficient indicates the *size* (i.e., slope) of the response [30]. The plots are grouped according to which replicates were included in the regression model. Plots under the heading "Replicate 1&2" were generating using all the data from both replicates in the model, whereas "Replicate 1" and "Replicate 2" plots were generated for each replicate separately. Table 4 summarizes the results with all data included.

In Figure 9, the dashed line marks the LogWorth threshold of 1.3, where LogWorth>1.3 (p-value<0.05) is required for a statistical significance level α = 0.05 [31]. From 30-60% UHSLA, the LogWorth of both input factors is consistently above the threshold. I.e., there is strong evidence to suggest that laser power and interlayer delay influenced the as-built hardness of these alloys. For compositions above and below, the LogWorth sometimes falls below the significance threshold depending on which replicates are included in the linear regression model. I.e., the evidence that the studied inputs caused the hardness variations in these alloys is generally not as strong. Interestingly, replicate 1 shows higher statistical significance for interlayer delay (blue line) compared to laser power (red line) for all compositions, while replicate 2 shows the opposite.
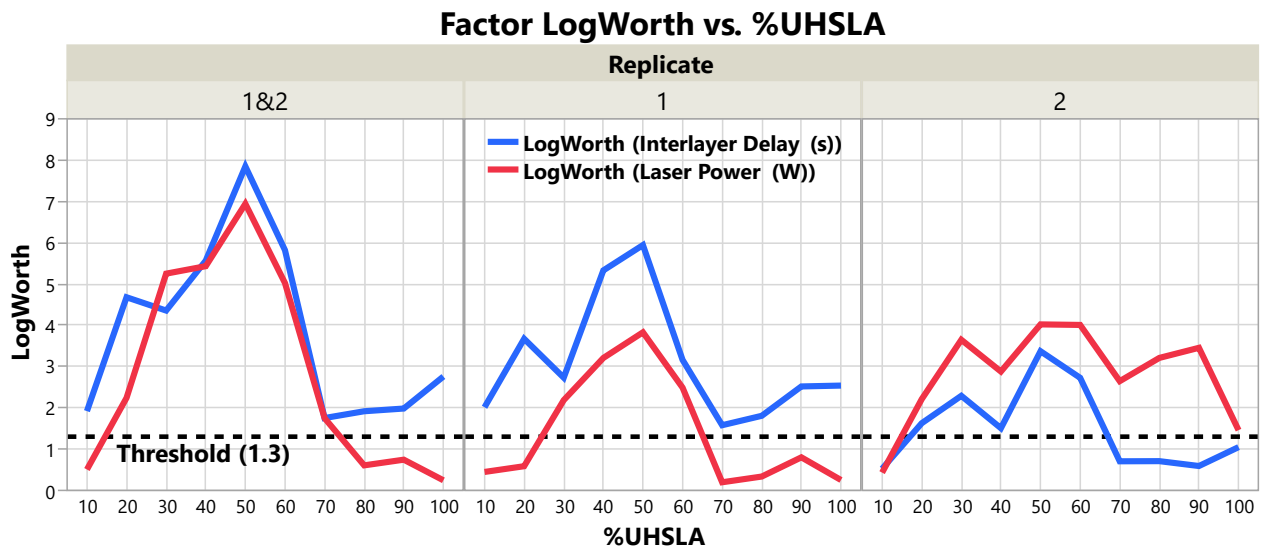

Figure 9. LogWorth of interlayer delay and laser power; grouped by included replicate(s).

The scaled coefficients are generally positive for interlayer delay and negative for laser power (Figure 10). I.e., *increasing* interlayer delay and *decreasing* laser power led to an *increase* in hardness. This can be explained based on cooling rates. With a longer time delay between layers, each layer has more time to cool before the next layer is added. This increases the temperature gradient during cooling of each layer, which in turn increases the cooling rate [2]. Similarly, at a constant scan speed, a lower laser power leads to an increase in the cooling rate [8]. In general, higher cooling rates lead to finer grains [8, 19] and a higher likelihood that the microstructure will transform to martensite [35]. Both of these factors lead to increased resistance to deformation, i.e., an increase in strength and hardness [35]. Note replicate 1 shows hardness correlating positively with laser power for 80-100% UHSLA, which is opposite the normal trend. Importantly, however, the LogWorth of this response is well below the significance threshold of 1.3, so no firm conclusions can be drawn from this behavior.
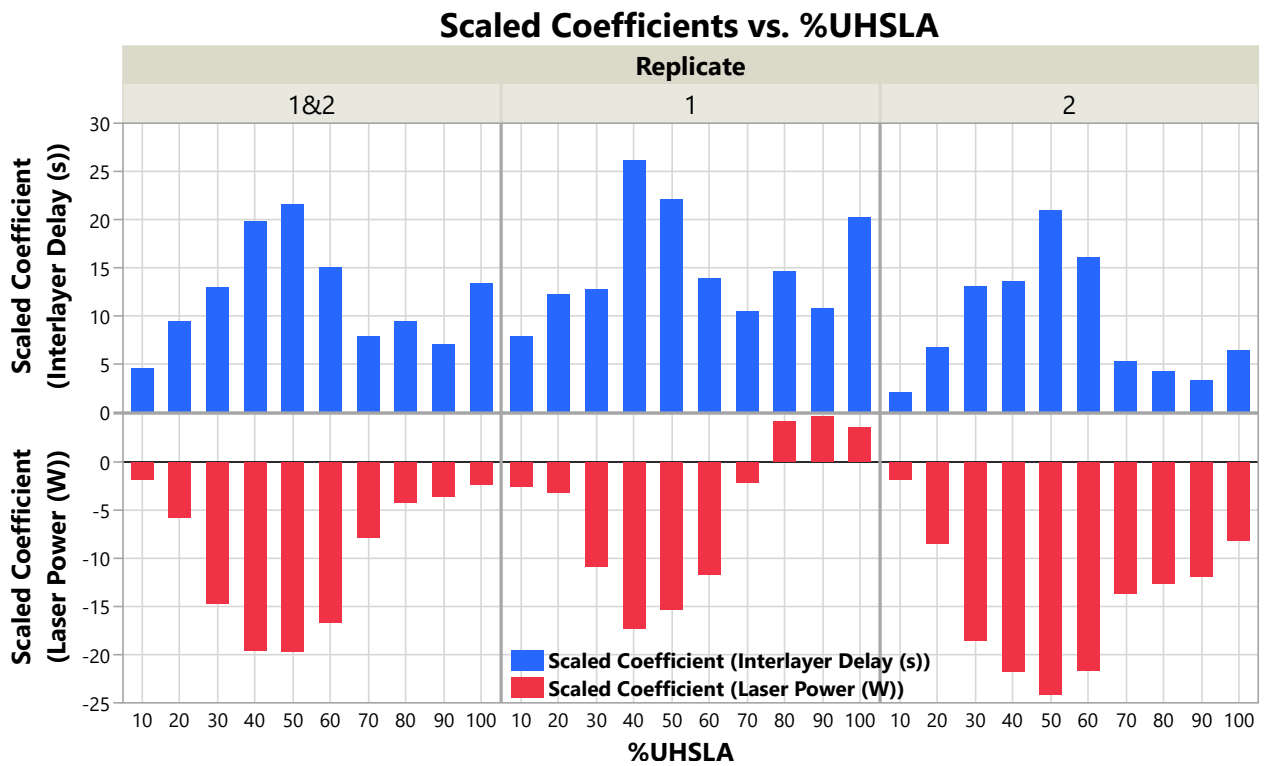

Figure 10. Scaled coefficients of interlayer delay and laser power; grouped by included replicate(s).

The magnitudes of the scaled coefficients, representing the size of the hardness response to the input factors, follow a similar pattern as the standard deviations from Figure 8. Referring to Figure 10 with both replicates in the model (left plot), the impacts of laser power and interlayer delay peak at 40-50% UHSLA, decreasing at UHSLA contents above and below. The plots for each individual replicate show similar trends. Replicate 1 shows additional peaks in the response to interlayer delay at 80% and 100% UHSLA (relative to the neighboring compositions), which likely contributed to the corresponding local peaks in the standard deviation. These peaks are smaller than those of 40-50% UHSLA. Replicate 2 shows a clearer drop in the response to interlayer delay as the UHSLA content increases above 60%. Replicate 1 generally shows a stronger response to interlayer delay, whereas replicate 2 shows a stronger response to laser power.

Table 4. LogWorth (LW) and scaled coefficients (SC) with both replicates included in the model.

%UHSLA	10	20	30	40	50	60	70	80	90	100
Interlayer Delay LW	1.92	4.68	4.36	5.57	7.85	5.82	1.75	1.92	1.98	2.76
Laser Power LW	0.51	2.24	5.25	5.43	6.94	5.02	1.75	0.61	0.74	0.25
Interlayer Delay SC	4.56	9.49	12.96	19.87	21.58	15.02	7.87	9.40	7.02	13.37
Laser Power SC	-1.78	-5.81	-14.73	-19.54	-19.70	-16.65	-7.87	-4.22	-3.58	-2.31

The standard deviations correlate fairly well with the scaled coefficients, which seems to indicate that the linear regression models were decently effective in explaining the observed hardness variations. Cases in which the LogWorth fell below the significance threshold may indicate other sources of variation which the models did not account for. It is not entirely clear what caused the few discrepancies between the two replicates, although such discrepancies are not surprising due to the complexity of the L-DED process. There were undoubtedly additional noise factors at play, such as particle size variations, imperfections in the in-situ mixing process, and potential reheating of previous deposits, to name a few. As mentioned in the Temperature History section, it is possible that the experimental run order had a degree of influence on the hardness since multiple samples were deposited on a single substrate for each composition. The deposition of replicate 2 samples might have caused tempering in some of the adjacent replicate 1 samples, possibly contributing additional sensitivities to replicate 1.

Microstructure Analysis

The microstructural phases play a critical role in interpreting the observed sensitivities. Figures 11 and 12 provide optical micrographs for compositions containing 10-50% and 60-100% UHSLA, respectively. Each column corresponds to a different composition. The top row (blue) corresponds to a laser power of 650 W and interlayer delay of 11 seconds, while bottom row (orange) corresponds to a laser power of 1050 W and interlayer delay of 1 second. As previously mentioned, lower laser powers and longer interlayer delays tend to lead to higher cooling rates [2, 8]. Hence, the top and bottom rows presumably represent the highest and lowest cooling rates, respectively, among the studied factor levels. Note all the images in Figures 11-13 were taken from replicate 2 at locations near the 5th hardness indentation, i.e., roughly 2.5 mm above the substrate surface (refer to Figure 5d). Images from replicate 1 were generally in good agreement with those from replicate 2. Within each deposit, layers near the top exhibited larger prior-austenite grains due to the lower cooling rates farther from the substrate [8]. The microstructural phases stood out more clearly in these regions, hence the reason for using images near the top of the deposits.

Referring to Figure 11, the compositions containing 10% and 20% UHSLA exhibit a ferrite structure. At lower cooling rates (bottom images), some acicular ferrite can be observed, particularly for 20% UHSLA as evidenced by the needle-like Fe_3C carbides (dark color) present in the microstructure. The compositions containing 30-50% UHSLA exhibit an interesting contrast between their microstructures at higher vs. lower cooling rates. Samples undergoing higher cooling rates consist of primarily lath martensite, while those undergoing lower cooling rates consist of primarily upper bainite as evidenced by the Fe_3C carbides (dark color) precipitated between the ferrite laths (light color) and by the feathery appearance [37]. Referring to Figure 12, 60% UHSLA
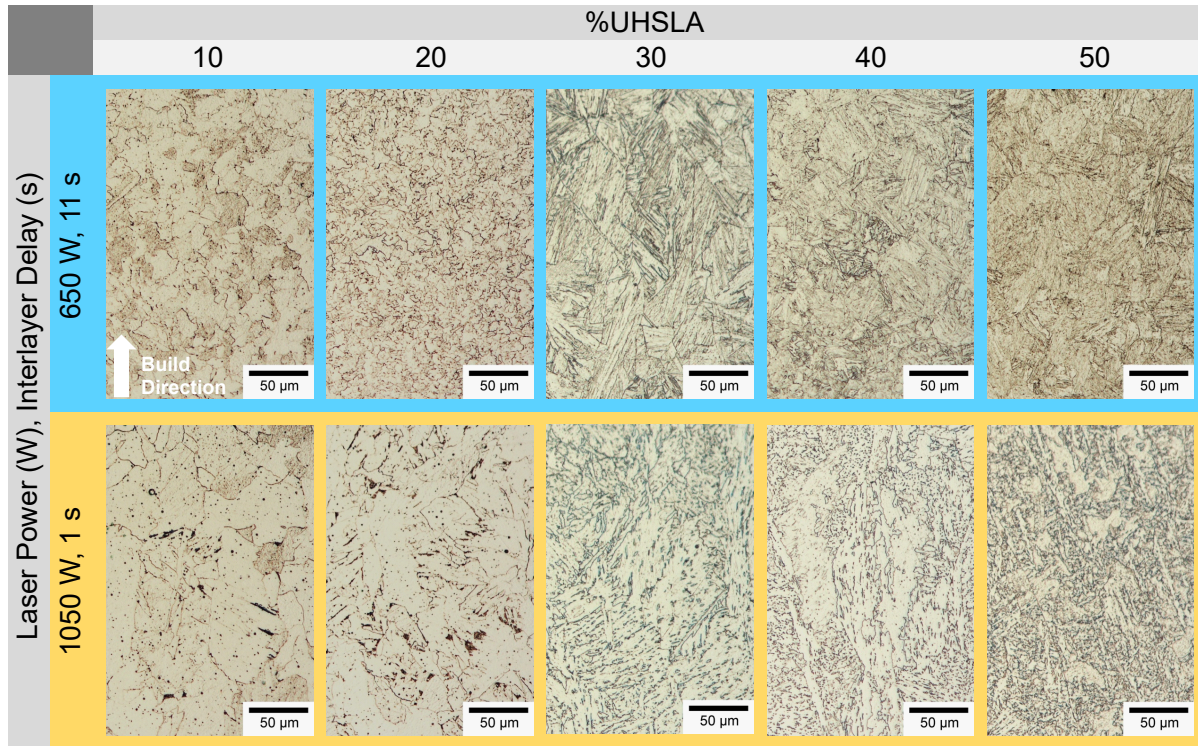
Figure 11. Optical micrographs - 10%-50% UHSLA.

exhibits a similar contrast in which the higher cooling rate appears to produce lath martensite, while the lower cooling rate appears to produce a mixed microstructure of bainite and martensite. Such fluctuations between lath martensite and upper bainite may explain the high hardness sensitivity in alloys containing 30-60% UHSLA, peaking at 40-50% UHSLA.

Referring to Figure 12, a significant change in the behavior can be seen once the composition reaches 70% UHSLA and above, in that the alloys containing 70-100% UHSLA exhibit lath martensite structures at both higher and lower cooling rates. The microstructures at faster cooling rates are more refined, with smaller prior-austenite grains and finer martensite laths. Note the dendritic solidification structures oriented along the build direction, evident in some of the images at lower cooling rates. Despite the differences, a martensitic structure appears to dominate in each case, which may explain the generally lower hardness sensitivity of these alloys.

Figure 13 provides SEM images of 70-100% UHSLA at 5000X magnification. A key feature which can be seen in the images for 80-100% UHSLA is the presence of auto-tempered martensite bands at lower cooling rates. Auto-tempering is known to occur in steels having relatively high martensite start (Ms) temperatures, typically low-alloy/low-carbon steels. In such steels, the first-formed martensite can be tempered during initial cooling under if the cooling rate is sufficiently low [38]. The auto-tempered regions appear as dark packets containing small, white carbide precipitates (circled in Figure 13), while the untempered martensite laths appear smoother. Notably, the samples deposited with faster cooling rates show little auto-tempering compared to those with lower cooling rates. Such differences may be a source of hardness sensitivity.
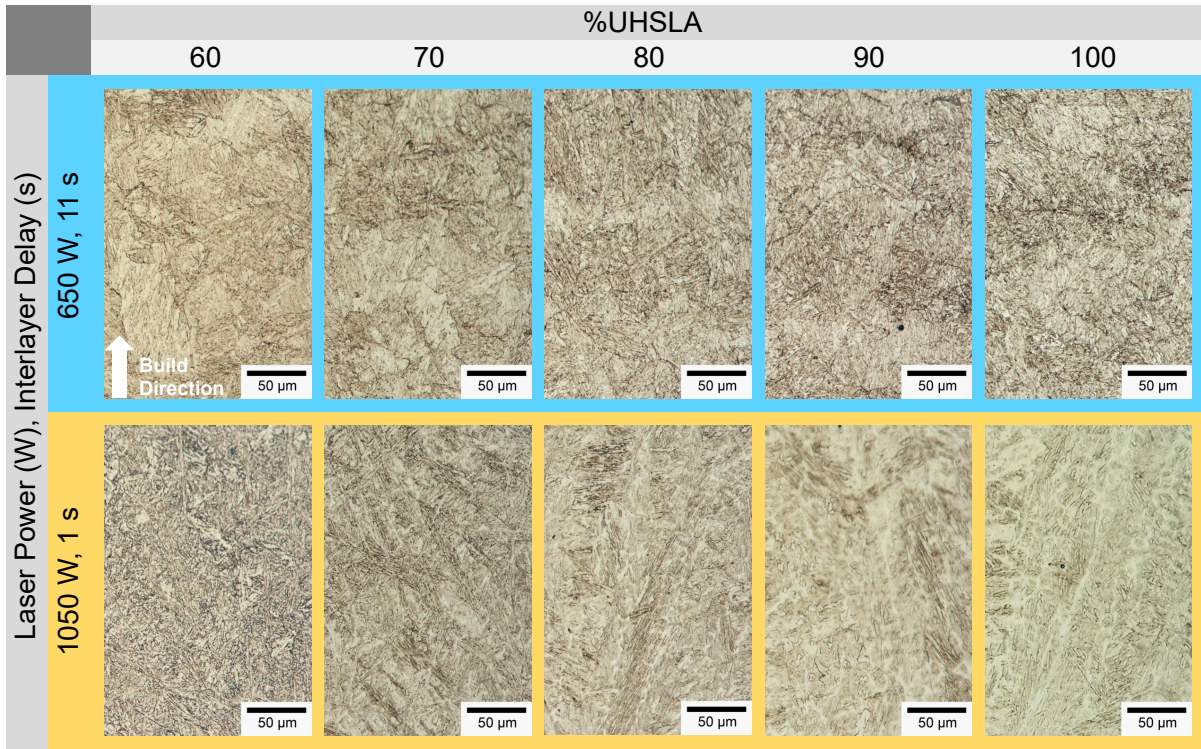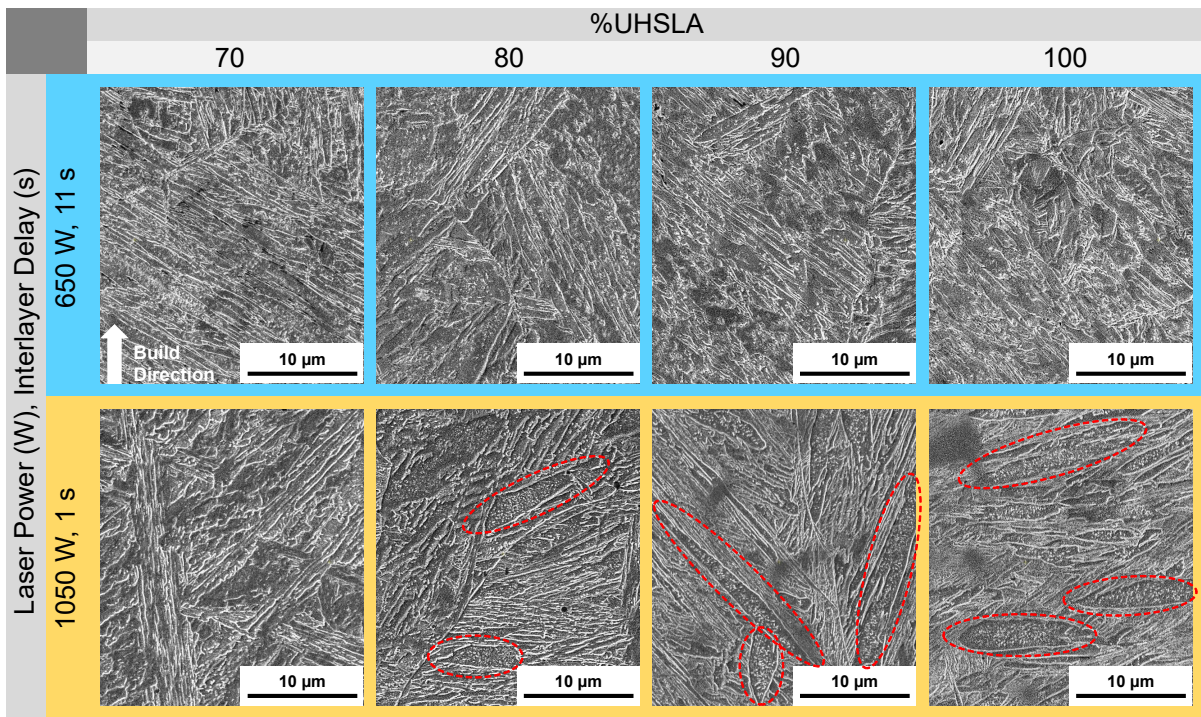
Figure 12. Optical micrographs - 60%-100% UHSLA.

Figure 13. SEM micrographs - 70%-100% UHSLA (circles highlight auto-tempered martensite).

Discussion

As expected, the mean hardness increased fairly linearly with increasing UHSLA content, beginning at ~128 HV for 10% UHSLA and increasing to ~488 HV for 100% UHSLA. The standard deviations in the hardness readings were relatively high for alloys containing 30-60% UHSLA, peaking at 40-50% UHSLA. This behavior accompanied phase fluctuations between lath martensite and upper bainite depending on the cooling rate resulting from a set of processing parameters. Lower alloy contents (10-20%) transformed primarily to ferrite, while higher contents (70-100%) transformed to lath martensite, with bands of auto-tempered martensite prevalent at lower cooling rates. These alloys generally exhibited lower hardness variability than those fluctuating between martensite and bainite. To compare, the standard deviations for 10/40/50/70/90% UHSLA were 11/34/33/22/18 HV, respectively. With the possible exception of 100% UHSLA, which exhibited a relatively high standard deviation of 28 HV, the results seem to indicate that martensite/bainite fluctuations are most detrimental to the robustness of as-built hardness, while the impacts of auto-tempering, grain sizes, and other factors are not as severe.

The trend in the standard deviation corresponded relatively closely to the trends in the scaled coefficients for laser power and interlayer delay time, indicating the standard deviation was a decent indicator of the hardness response to the input factors. In replicate 1 of the experiment, additional peaks in the sensitivity to interlayer delay time were observed at 80% and 100% UHSLA (relative to neighboring compositions). This led to corresponding peaks in the standard deviation at these compositions, although these peaks were smaller than those at 40-50% UHSLA. It is possible that a degree of tempering occurred in some samples from replicate 1 as samples of replicate 2 were deposited nearby, which might have contributed to the hardness variations in replicate 1. The LogWorth plots indicated strong statistical evidence (p-value<0.05) that both laser power and interlayer delay time had an influence on the hardness in alloys containing 30-60% UHSLA. For compositions above and below, the LogWorth sometimes fell below the significance threshold depending on which replicates were included in the linear regression model, possibly indicating other sources of hardness variation which the models did not account for.

To identify an optimal alloy, robustness considerations must be balanced with the desired mechanical performance and other factors such a printability. The alloy containing 10% UHSLA exhibited good robustness due to consistently obtaining ferrite, and its very low carbon content lends to good printability. Its very low hardness, however, renders it useless for high-hardness, high-strength applications. The alloys containing 30-60% UHSLA suffered from martensite/bainite fluctuations, leading to low robustness. At 100% UHSLA, the hardness was very high, which may indicate excellent high-strength performance. Its higher carbon content, however, may increase its susceptibility to solidification cracking. Additionally, 100% UHSLA was found to exhibit relatively high hardness sensitivity in experimental replicate 1. At 70% UHSLA, the alloy content was just high enough to ensure transformation to martensite, rendering high hardness (418 HV/42 HRC) and good robustness while avoiding increased hot cracking susceptibility at higher carbon contents. Assuming optimization criteria balancing good robustness, good printability, and high hardness, the alloy containing 70% UHSLA seems to exhibit a favorable combination of properties.

Conclusions

This work investigated the effect of steel alloy composition on the robustness of as-built hardness to process variations in L-DED. In-situ blending of UHSLA steel and pure iron powders produced 10 studied mixtures ranging from 10% to 100% UHSLA by mass. Vickers hardness sensitivities to laser power and interlayer delay time were analyzed through multiple linear regression. Observed microstructures were correlated with the results. Key conclusions are elaborated below.

1. The hardness sensitivity peaked at 40-50% UHSLA, corresponding to phase fluctuations between lath martensite and upper bainite depending on the cooling rate. Lower alloy contents (10-20%) transformed primarily to ferrite, while higher contents (70-100%) obtained lath martensite, with bands of auto-tempered martensite at lower cooling rates; these alloys generally exhibited improved robustness by avoiding martensite/bainite fluctuations.

2. 70% UHSLA may be a favorable balance at which the alloy content is just high enough to ensure transformation to martensite, rendering high hardness (418 HV/42 HRC) and good robustness while avoiding increased hot cracking susceptibility at higher carbon contents.

3. EDS analyses indicated the in-situ mixing strategy was effective in producing approximately the target compositions. The novel rotary deposition scheme enabled rapid collection of a large amount of hardness data. A possible downside to this setup is that it allowed for the potential tempering of previous samples as new samples were deposited nearby. This might be considered a benefit, however, as it allows additional noise factors to be investigated.

Sensitivity analyses of tensile properties and impact toughness would be a valuable addition to the hardness sensitivities presented in this paper. The in-situ mixing strategy could be expanded to allow each element's fraction to be tuned individually. A thorough investigation into the individual effects of auto-tempering, cyclic tempering, and grain sizes would provide a more comprehensive explanation of the observed sensitivities. In-situ monitoring of cooling rates would allow for a more direct evaluation of the factors influencing the microstructures.

In summary, this work demonstrated the efficacy of a methodology integrating in-situ powder mixing with a novel rotary deposition setup, statistical analyses, and microstructure analyses to investigate process robustness over a composition space in L-DED.

Acknowledgments

References

[1] S. Sun, Milan Brandt, and M. Easton. *Powder bed fusion processes: An overview*, pages 55–77. Elsevier Inc., 2017. ISBN 9780081004340. doi: 10.1016/B978-0-08-100433-3.00002-6.

[2] Scott M. Thompson, Linkan Bian, Nima Shamsaei, and Aref Yadollahi. An overview of direct laser deposition for additive manufacturing; part i: Transport phenomena, modeling and diagnostics. *Additive Manufacturing*, 8:36–62, 10 2015. ISSN 22148604. doi: 10.1016/j.addma.2015.07.001.

[3] Ana Vafadar, Ferdinando Guzzomi, Alexander Rassau, and Kevin Hayward. Advances in metal additive manufacturing: a review of common processes, industrial applications, and current challenges. *Applied Sciences*, 11(3):1213, 2021.

[4] J. P. Oliveira, T. G. Santos, and R. M. Miranda. Revisiting fundamental welding concepts to improve additive manufacturing: From theory to practice. *Progress in Materials Science*, 107, 1 2020. ISSN 00796425. doi: 10.1016/j.pmatsci.2019.100590.

[5] A. T. Clare, R. S. Mishra, M. Merklein, H. Tan, I. Todd, L. Chechik, J. Li, and M. Bambach. Alloy design and adaptation for additive manufacture. *Journal of Materials Processing Technology*, 299, 1 2022. ISSN 09240136. doi: 10.1016/j.jmatprotec.2021.117358.

[6] H.L. Wei, T. Mukherjee, W. Zhang, J.S. Zuback, G.L. Knapp, A. De, and T. DebRoy. Mechanistic models for additive manufacturing of metallic components. *Progress in Materials Science*, 116:100703, 2 2021. ISSN 00796425. doi: 10.1016/j.pmatsci.2020.100703.

[7] M. A. Ackers, O. M.D.M. Messé, and U. Hecht. Novel approach of alloy design and selection for additive manufacturing towards targeted applications. *Journal of Alloys and Compounds*, 866, 6 2021. ISSN 09258388. doi: 10.1016/j.jallcom.2021.158965.

[8] Nima Shamsaei, Aref Yadollahi, Linkan Bian, and Scott M Thompson. An overview of direct laser deposition for additive manufacturing; part ii: Mechanical behavior, process parameter optimization and control. *Additive manufacturing*, 8:12–35, 2015.

[9] Shaun Cooke, Keivan Ahmadi, Stephanie Willerth, and Rodney Herring. Metal additive manufacturing: Technology, metallurgy and modelling. *Journal of Manufacturing Processes*, 57:978–1003, 2020.

[10] Chen Zhang, Junkai Zhu, Huai Zheng, Hui Li, Sheng Liu, and Gary J Cheng. A review on microstructures and properties of high entropy alloys manufactured by selective laser melting. *International Journal of Extreme Manufacturing*, 2(3):032003, 2020.

[11] Srinath Gudur, Vishwanath Nagallapati, Sagar Pawar, Gopinath Muvvala, and Suryakumar Simhambhatla. A study on the effect of substrate heating and cooling on bead geometry in wire arc additive manufacturing and its correlation with cooling rate. *Materials Today: Proceedings*, 41:431–436, 2021.

[12] Zhuo Wang, Pengwei Liu, Yaohong Xiao, Xiangyang Cui, Zhen Hu, and Lei Chen. A data-driven approach for process optimization of metallic additive manufacturing under uncertainty. *Journal of Manufacturing Science and Engineering, Transactions of the ASME*, 141, 8 2019. ISSN 15288935. doi: 10.1115/1.4043798.

[13] Wenping Gong, Sara Khoshnevisan, and C. Hsein Juang. Gradient-based design robustness measure for robust geotechnical design. *Canadian Geotechnical Journal*, 51:1331–1342, 11 2014. ISSN 12086010. doi: 10.1139/cgj-2013-0428.

[14] Gehendra Sharma, Janet K Allen, and Farrokh Mistree. Classification and execution of coupled decision problems in engineering design for exploration of robust design solutions. In *International Design Engineering Technical Conferences and Computers and Information in Engineering Conference*, volume 59186, page V02AT03A019. American Society of Mechanical Engineers, 2019.

[15] Xin Wang and Wei Xiong. Uncertainty quantification and composition optimization for alloy additive manufacturing through a calphad-based icme framework. *npj Computational Materials*, 6, 12 2020. ISSN 20573960. doi: 10.1038/s41524-020-00454-9.

[16] Luke Johnson, Mohamad Mahmoudi, Bing Zhang, Raiyan Seede, Xueqin Huang, Janine T. Maier, Hans J. Maier, Ibrahim Karaman, Alaa Elwany, and Raymundo Arróyave. Assessing printability maps in additive manufacturing of metal alloys. *Acta Materialia*, 176:199–210, 9 2019. ISSN 13596454. doi: 10.1016/j.actamat.2019.07.005.

[17] Zhongji Sun, Yan Ma, Dirk Ponge, Stefan Zaefferer, Eric A. Jägle, Baptiste Gault, Anthony D. Rollett, and Dierk Raabe. Thermodynamics-guided alloy and process design for additive manufacturing. *Nature Communications*, 13, 12 2022. ISSN 20411723. doi: 10.1038/s41467-022-31969-y.

[18] C. S. Wright, M. Youseffi, S. P. Akhtar, T. H.C. Childs, C. Hauser, P. Fox, and J. Xie. Selective laser melting of prealloyed high alloy steel powder beds. In *Materials science forum*, volume 514-516, pages 516–523. Trans Tech Publications Ltd, 2006. ISBN 9780878494026. doi: 10.4028/www.scientific.net/msf.514-516.516.

[19] Duyao Zhang, Arvind Prasad, Michael J. Bermingham, Carmelo J. Todaro, Michael J. Benoit, Mitesh N. Patel, Dong Qiu, David H. StJohn, Ma Qian, and Mark A. Easton. Grain refinement of alloys in fusion-based additive manufacturing processes. *Metallurgical and Materials Transactions A: Physical Metallurgy and Materials Science*, 51:4341–4359, 9 2020. ISSN 10735623. doi: 10.1007/s11661-020-05880-4.

[20] M. Haines, A. Plotkowski, C. L. Frederick, E. J. Schwalbach, and S. S. Babu. A sensitivity analysis of the columnar-to-equiaxed transition for ni-based superalloys in electron beam additive manufacturing. *Computational Materials Science*, 155:340–349, 12 2018. ISSN 09270256. doi: 10.1016/j.commatsci.2018.08.064.

[21] Amit Bandyopadhyay, Kellen D. Traxel, Melanie Lang, Michael Juhasz, Noam Eliaz, and Susmita Bose. Alloy design via additive manufacturing: Advantages, challenges, applications and perspectives. *Materials Today*, 52:207–224, 1 2022. ISSN 18734103. doi: 10.1016/j.mattod.2021.11.026.

[22] Kenneth S Vecchio, Olivia F Dippo, Kevin R Kaufmann, and Xiao Liu. High-throughput rapid experimental alloy development (ht-read). *Acta Materialia*, 221:117352, 2021.

[23] Helene Knoll, Sörn Ocylok, Andreas Weisheit, Hauke Springer, Eric Jägle, and Dierk Raabe. Combinatorial alloy design by laser additive manufacturing. *Steel Research International*, 88, 8 2017. ISSN 16113683. doi: 10.1002/srin.201600416.

[24] Vaishak Ramesh Sagar, Samuel Lorin, Kristina Warmefjord, and Rikard Soderberg. A robust design perspective on factors influencing geometric quality in metal additive manufacturing. *Journal of Manufacturing Science and Engineering, Transactions of the ASME*, 143, 7 2021. ISSN 15288935. doi: 10.1115/1.4048742.

[25] Zhen Hu and Sankaran Mahadevan. Uncertainty quantification and management in ad-

ditive manufacturing: current status, needs, and opportunities. *International Journal of Advanced Manufacturing Technology*, 93:2855–2874, 11 2017. ISSN 14333015. doi: 10.1007/s00170-017-0703-5.

[26] D. R. Feenstra, A. Molotnikov, and N. Birbilis. Utilisation of artificial neural networks to rationalise processing windows in directed energy deposition applications. *Materials and Design*, 198, 1 2021. ISSN 18734197. doi: 10.1016/j.matdes.2020.109342.

[27] T. Q.D. Pham, T. V. Hoang, X. V. Tran, S. Fetni, L. Duchêne, H. S. Tran, and A. M. Habraken. Uncertainty quantification in the directed energy deposition process using deep learning-based probabilistic approach. In *Key Engineering Materials*, volume 926 KEM, pages 323–330. Trans Tech Publications Ltd, 2022. ISBN 9783035717594. doi: 10.4028/p-j9chvq.

[28] Rúben Tome Jardin, Víctor Tuninetti, Jérôme Tchoufang Tchuindjang, Neda Hashemi, Raoul Carrus, Anne Mertens, Laurent Duchêne, Hoang Son Tran, and Anne Marie Habraken. Sensitivity analysis in the modeling of a high-speed, steel, thin wall produced by directed energy deposition. *Metals*, 10:1–24, 11 2020. ISSN 20754701. doi: 10.3390/met10111554.

[29] Evangelos C Alexopoulos. Introduction to multivariate regression analysis. *Hippokratia*, 14 (Suppl 1):23, 2010.

[30] Scaled estimates and the coding of continuous terms, 2018. JMP Statistical Discovery. https://www.jmp.com/support/help/14/scaled-estimates-and-the-coding-of-continuous-te.shtml.

[31] Bruce L. Bowerman, Richard T. O'Connell, and Emily S. Murphree. *Regression Analysis: Unified Concepts, practical applications, and computer implementation*. Business Expert Press, 1st edition, 2015.

[32] ASTM E92-17 - Standard Test Methods for Vickers Hardness and Knoop Hardness of Metallic Materials. 2017. doi: 10.1520/E0092-17. www.astm.org.

[33] Abhilash Kiran, Martina Koukolíková, Jaroslav Vavřík, Miroslav Urbánek, and Jan Džugan. Base plate preheating effect on microstructure of 316l stainless steel single track deposition by directed energy deposition. *Materials*, 14, 9 2021. ISSN 19961944. doi: 10.3390/ma14185129.

[34] ASTM E140-12b(2019) - Standard Hardness Conversion Tables for Metals Relationship Among Brinell Hardness, Vickers Hardness, Rockwell Hardness, Superficial Hardness, Knoop Hardness, Scleroscope Hardness, and Leeb Hardness. 2019. doi: 10.1520/E0140-12R19E01. www.astm.org.

[35] Harshad Bhadeshia and Robert Honeycombe. *Steels: Microstructure and properties*. Elsevier, 4 edition, 2017.

[36] Kiarash Tanha, Neda Mohammadi, and Leila Janani. P-value: What is and what is not. *Medical Journal of the Islamic Republic of Iran*, 31:65, 2017.

[37] Zhi-Gang Yang and Hong-Sheng Fang. An overview on bainite formation in steels. *Current Opinion in Solid State and Materials Science*, 9(6):277–286, 2005.

[38] Shashank Ramesh Babu, Tuomo Nyyssönen, Matias Jaskari, Antti Järvenpää, Thomas Paul Davis, Sakari Pallaspuro, Jukka Kömi, and David Porter. Observations on the relationship between crystal orientation and the level of auto-tempering in an as-quenched martensitic steel. *Metals*, 9, 12 2019. ISSN 20754701. doi: 10.3390/met9121255.